

# Cervical Optical Coherence Tomography Image Classification Based on Contrastive Self-Supervised Texture Learning

Kaiyi Chen, Qingbin Wang, and Yutao Ma

*School of Computer Science*

*Wuhan University*

*Wuhan, China*

{chris, qbwang, ytma}@whu.edu.cn

**Abstract—Background:** Cervical cancer seriously affects the health of the female reproductive system. Optical coherence tomography (OCT) emerges as a non-invasive, high-resolution imaging technology for cervical disease detection. However, OCT image annotation is knowledge-intensive and time-consuming, which impedes the training process of deep-learning-based classification models. **Objective:** This study aims to develop a computer-aided diagnosis (CADx) approach to classifying *in-vivo* cervical OCT images based on self-supervised learning. **Methods:** Besides high-level semantic features extracted by a convolutional neural network (CNN), the proposed CADx approach leverages unlabeled cervical OCT images' texture features learned by contrastive texture learning. We conducted ten-fold cross-validation on the OCT image dataset from a multi-center clinical study on 733 patients from China. **Results:** In a binary classification task for detecting high-risk diseases, including high-grade squamous intraepithelial lesion (HSIL) and cervical cancer, our method achieved an area-under-the-curve (AUC) value of  $0.9798 \pm 0.0157$  with a sensitivity of  $91.17 \pm 4.99\%$  and a specificity of  $93.96 \pm 4.72\%$  for OCT image patches; also, it outperformed two out of four medical experts on the test set. Furthermore, our method achieved a 91.53% sensitivity and 97.37% specificity on an external validation dataset containing 287 3D OCT volumes from 118 Chinese patients in a new hospital using a cross-shaped threshold voting strategy. **Conclusion:** The proposed contrastive-learning-based CADx method outperformed the end-to-end CNN models and provided better interpretability based on texture features, which holds great potential to be used in the clinical protocol of “see-and-treat.”

**Keywords**—cervical cancer, self-supervised learning, local binary pattern, optical coherence tomography, visualization

## I. INTRODUCTION

Cervical cancer ranked fourth for both incidence and mortality among females in 2018 [1]. About 570,000 new cases and 311,000 deaths from cervical cancer occurred in 2018 [2], and over 80% of them occurred in poor and developing countries. It has been recognized that almost all cases of cervical cancer are caused mainly by the human papillomavirus (HPV). Fortunately, the World Health Organization (WHO) has treated cervical cancer as a public health problem and adopted specific strategies to accelerate the elimination of cervical cancer, including effective HPV vaccination, cervical screening, and timely treatment of precancerous lesions [3].

There are several standard clinical screening methods for cervical disease detection, such as the HPV test, thin-prep cytologic test (TCT), and colposcopy. However, these methods have their respective disadvantages [4], [5]. The cervical biopsy with histopathological confirmation is the gold standard to diagnose cervical diseases. However, it is invasive and time-consuming; besides, the rate of missed diagnosis is relatively high due to biopsy sampling errors. Therefore, developing rapid, non-invasive, effective, and intelligent screening

and diagnostic approaches [6] is necessary to achieve the WHO 2030 targets.

Optical coherence tomography (OCT) [7] is an emerging non-invasive three-dimensional (3D) imaging technology developed in the early 1990s. An OCT system uses light waves to obtain high-resolution, cross-sectional images in biological systems rapidly. Currently, OCT has widely been applied in ophthalmology, cardiology, and other fields of clinical medicine. Moreover, recent studies of OCT imaging on the cervix [5], [8], [9], [10] have shown that this technology can capture histomorphological features of cervical tissue *ex vivo* and *in vivo* and thus enables pathologists or gynecologists to make a proper diagnosis. Unfortunately, most pathologists and gynecologists do not get familiar with cervical OCT images, implying a sharp learning curve. Therefore, we need to develop intelligent computer-aided diagnosis (CADx) approaches to help gynecologists analyze cervical OCT images efficiently.

In recent years, deep-learning-based CADx approaches for medical images with different modalities have achieved better results than traditional machine learning algorithms. The same is true in analyzing cervical tissue images. For example, Almubarak *et al.* [11] exploited multi-scale features to classify histology images from cervical tissue samples on a small-scale dataset and achieved an accuracy of 77.25%. Bhargava *et al.* [12] employed support vector machine (SVM), k-nearest neighbor, and artificial neural network (ANN) models to train Pap smear image classifiers using hand-craft features. They found that the ANN-based classifier performed best in the test on a small-scale dataset. Kudva *et al.* [13] presented a hybrid transfer learning approach for cervical cancer screening using two convolutional neural networks (CNNs): AlexNet and VGG-16. Priya *et al.* [14] proposed a heuristic and ANN-based classification model for early cervical cancer screening using linear SVM. Alyafeai *et al.* [15] proposed a fully automated pipeline for cervical cancer classification of cervigram images, consisting of two pre-trained deep learning models. Li *et al.* [16] proposed a deep learning framework for identifying cervical intraepithelial neoplasia (CIN) and cervical cancer using time-lapsed colposcopic images. They tested the proposed framework's performance and found that it was comparable to an in-service colposcopist.

Training CNN-based models for medical image analysis requires large amounts of labeled image data. Due to insufficient training data, many CADx approaches cannot reach the desired performance level, especially when dealing with new image datasets [17]. To address the above problem, researchers proposed self-supervised learning methods to leverage unlabeled data available. As an unsupervised learning approach for representation learning without manual data labels, self-supervised learning has achieved great success on images and

texts. Recently, it was also used to alleviate the vital requirement of data annotation for medical images. For example, Zhu *et al.* [18] proposed a pretext task that sorts slices extracted from 3D computed tomography (CT) and magnetic resonance imaging (MRI) volumes and fine-tuned a 3D neural network model on a small amount of annotated data. Taleb *et al.* [19] conducted a similar study and released their implementations as an open-source library. Chen *et al.* [20] proposed a context restoration strategy for self-supervised learning to learn useful semantic features of three different types of medical images. However, most of the existing self-supervised learning methods for medical images focus on high-level semantic features rather than the local texture information beneficial for diagnosing gray-scale images, such as CT, MRI, and OCT.

OCT image annotation is also a labor-intensive and time-consuming procedure. Furthermore, few medical experts are familiar with this new technology. In this case, self-supervised learning is thus a proper solution to construct deep-learning-based OCT image classification models for cervical cancer screening and diagnosis. To this end, we develop a new CADx approach for cervical OCT images using contrastive self-supervised texture learning. Specifically, the proposed CADx approach leverages the local texture information and high-level semantic features extracted by a CNN model. As a result, we need only a small-scale dataset of labeled cervical OCT images to fine-tune the CNN model for image classification, reducing the burden on image annotation and facilitating our CADx approach's training process.

TABLE I. DEMOGRAPHIC INFORMATION OF PATIENTS [5]

Hospital	#Patients	Age (mean $\pm$ std)	HPV results	TCT results
The Third Affiliated Hospital of Zhengzhou University	350	38.67 $\pm$ 9.86	Positive: 281 Negative: 31 Untested: 38	Positive: 215 Negative: 63 Untested: 72
Liaoning Cancer Hospital and Institute	227	44.08 $\pm$ 8.38	Positive: 138 Negative: 84 Untested: 12	Positive: 69 Negative: 134 Untested: 24
Puyang Oilfield General Hospital	59	43.04 $\pm$ 8.06	Positive: 39 Negative: 3 Untested: 17	Positive: 39 Negative: 12 Untested: 8
Luohe Central Hospital	57	40.37 $\pm$ 10.05	Positive: 49 Negative: 8 Untested: 0	Positive: 36 Negative: 21 Untested: 0
Zhengzhou Jinshui District General Hospital	49	39.03 $\pm$ 12.47	Positive: 36 Negative: 2 Untested: 2	Positive: 9 Negative: 27 Untested: 4
Overall	733	40.85 $\pm$ 9.79	Positive: 536 Negative: 128 Untested: 69	Positive: 368 Negative: 257 Untested: 108

A 3D OCT volume from the point of a 12-hour clock on the cervix contains 10 or 20 frames, each corresponding to an *in-vivo* cervical OCT image. The class label of each 3D OCT volume was set according to the histopathology-confirmed diagnosis for the corresponding biopsy specimen. Due to biopsy sampling errors and image quality issues, we selected 1,256 3D OCT volumes from 699 patients, all of which match well with the corresponding hematoxylin and eosin (H&E) stained images. We then extracted patches of  $600 \times 600$  pixels that localize a local lesion from the whole OCT image. As with [5], [6], [8], this study defines mild inflammation (MI), ectropion (EP), and cyst (CY) as low-risk or negative, and high-grade squamous intraepithelial lesion (HSIL) (including CIN II and CIN III) and cervical cancer (CC) as high-risk or positive. Table II shows the statistics of the OCT image dataset.

TABLE II. STATISTICS OF EXPERIMENTAL DATASET

Size	MI	EP	CY	HSIL	CC	Total
#Patients	239	126	99	161	74	699
#Volumes	363	195	153	166	379	1,256
#Patches	3,172	2,464	2,067	5,539	731	13,973

In brief, the main contributions of this study are three-fold:

- We first introduce contrastive self-supervised learning to *in-vivo* cervical OCT image classification and develop a new CADx approach for cervical cancer screening and diagnosis.
- We define and specify a contrastive texture learning (CTL) strategy to learn texture features of unlabeled cervical OCT images, providing better interpretability for gynecologists or pathologists.
- We demonstrate that the CTL strategy outperforms the state-of-the-art contrastive learning method and can match four medical experts on an OCT image dataset from a multi-center clinical study.

## II. MATERIALS AND METHOD

### A. Data Collection

The OCT image dataset was collected from a multi-center clinical study using OCT to evaluate cervical lesions *in vivo* [5]. Seven hundred thirty-three gynecological outpatients were recruited in five hospitals in China from August 2017 to December 2019. The standard for patient recruitment is that one or both cervical screening results (i.e., HPV and TCT results) were positive. Each of the patients recruited for this multi-center clinical study was inspected with OCT and received colposcopy-directed cervical biopsy. Table I presents the demographic information of all the patients [5].

Besides, we collected 287 3D OCT volumes from 118 outpatients (2.43 points per patient) in the Second Xiangya Hospital of Central South University as an external validation dataset to evaluate our CADx approach's robustness, approved by the Ethics Committees of the hospital. All of the 118 patients (or their legal guardians) signed informed consent. Each OCT volume has a specific label from histopathology or radiology in the same hospital.

### B. Model Construction and Training

The core of our CADx approach is a multi-granularity OCT image classification model for patches, images, and 3D volumes. This classification model is structured and trained in a self-supervised learning manner. Self-supervised learning usually has two steps. First, it defines a specific pretext task to pre-train a model on a large-scale dataset of unlabeled data. The pretext task aims to learn representations for downstream tasks. Second, for specific downstream tasks, the pre-trained model is fine-tuned on a small-scale annotated dataset. Fig. 1 presents an overview of the classification model's construction and training process.

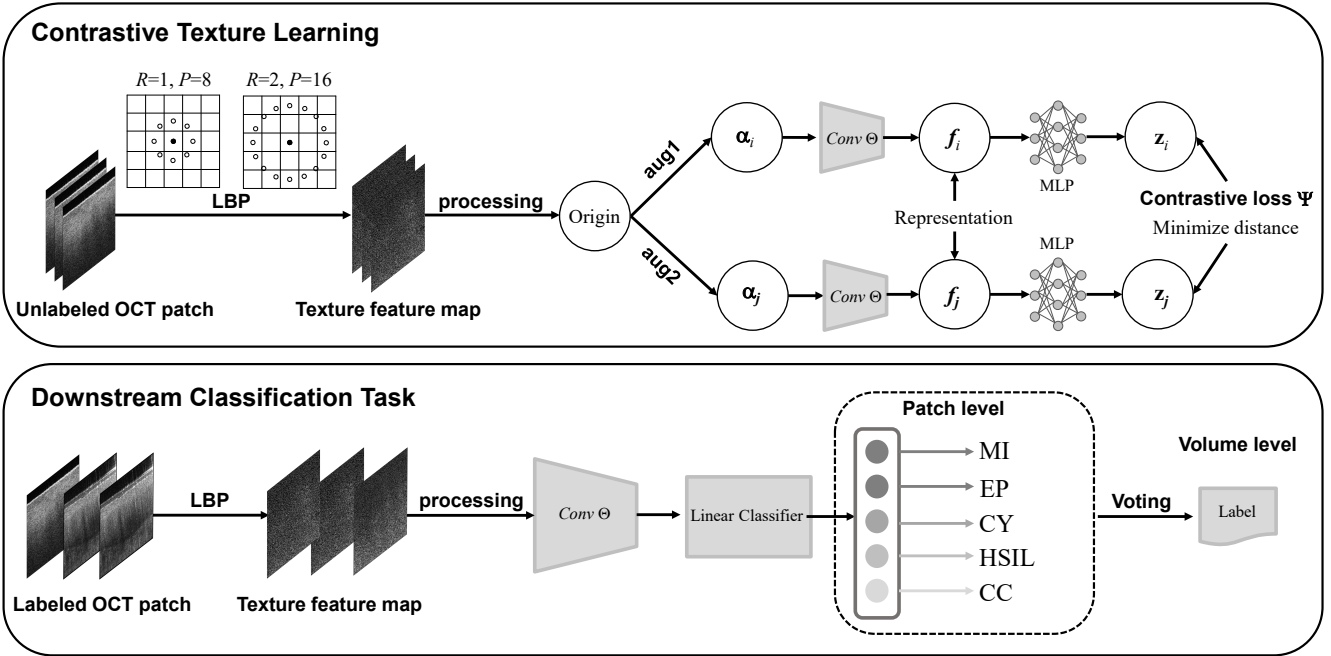


Fig. 1. The construction and training process of the classification model based on self-supervised learning.

**Pretext task definition.** We specify the pretext task for this study by CTL, which aims to build visual representations by learning to encode the similarity or difference between two texture feature maps. We first extract texture features from an input image because the texture features of gray-scale medical images are particularly prominent at the pixel level. For more details of the texture extraction algorithm, please refer to Subsection II.C. Then, we deal with texture feature maps by the standard min-max normalization method to avoid the local extremum. Otherwise, we use the standard zero-score method to normalize the input patches without extracting texture features. Finally, we generate a pair of new samples for each normalized texture feature map using data augmentation, such as random rotation and the vertical and horizontal flip augmentation, to provide richer features for CTL.

Due to the advantages of CNNs, we also model the CTL strategy by the CNN architecture. For example, suppose we build a CNN network denoted as  $Conv \Theta$ . Then, normalized texture feature maps with data augmentation are feed into the network to generate feature maps. For more details of the CTL loss function, please refer to Subsection II.D. In the pretext task, we employ a multilayer perceptron (MLP) to replace the original fully connected layer, called the projection head [21]. Thus, when performing the downstream classification task, the feature maps obtained by the network will be more generalized rather than biased towards distinguishing feature distributions of different classes of input images. Moreover, we use the batch normalization method for each CNN layer to avoid the internal covariate shift.

**Downstream task execution.** We fine-tune the pre-trained network  $Conv \Theta$  for the downstream classification task using a small amount of labeled data. Specifically, we replace the last fully connected layer of the network (i.e., the MLP) with a global average pooling (GAP) layer to meet the size requirement and reduce the computation load. Besides, our CADx method can highlight texture features of cervical diseases learned from cervical OCT images to interpret diagnoses better. For more details of image classification and visualization, please refer to Subsection II.E.

### C. Texture Extraction Algorithm

Ojala *et al.* [22] proposed a straightforward yet efficient approach to extract rotation invariant texture features from gray-scale images with local binary patterns (LBPs). Given an input image  $G$ , we characterize the spatial structure of local texture features by defining  $LBP_{P,R,G}$  as

$$LBP_{P,R,G} = \sum_{p=0}^{P-1} I_{[(g_p - g_c \geq 0)]} (g_p - g_c) 2^p, \quad (1)$$

where  $I(\cdot)$  is an indicator function,  $g_c$  is the gray value of the center pixel of the local neighborhood,  $g_p$  is the gray value of an equally spaced pixel on a circle of radius  $R$  ( $R > 0$ ), and  $P$  is the number of pixels on the circle.

The LBP part in Fig. 1 illustrates circularly symmetric neighbor sets for different combinations of  $P$  and  $R$ . If the center pixel corresponding to  $g_c$  is located at the origin (0,0), the coordinates of a pixel corresponding to  $g_p$  are given by  $(-R\sin(2\pi p/P), R\cos(2\pi p/P))$ . To maintain rotation invariance, we then define a unique identifier for a rotation-invariant LBP as

$$LBP_{P,R,G}^i = \min\{ROR(LBP_{R,R,G}, i) \mid i = 0, 1, \dots, P-1\}, \quad (2)$$

where  $ROR(\xi, i)$  performs shifting the binary bits of integer  $\xi$  rightward for  $i$  times. In this study, we set  $R = 4$  and  $P = 32$  to obtain the most distinguishable cervical OCT image texture features on the experimental dataset.

### D. CTL Loss Function

Contrastive learning is one of the most commonly-used pretext tasks in self-supervised learning. Its goal is to learn the similarity and the difference between various classes. Therefore, contrastive learning has widely been applied to build pre-training models using a large amount of unlabeled data. Given a randomly sampled mini-batch of  $B$  input samples (i.e., texture feature maps extracted by LBP), we generate  $2 \times B$  new samples using data augmentation. For each positive pair  $(i, j)$  of augmented samples from the same original input, we

treat the remaining  $2 \times (B - 1)$  augmented samples as negative samples. As shown in the contrastive loss part in Fig. 1, we define the CTL loss function  $\zeta$  of pair  $(i, j)$  as

$$\zeta_{i,j} = -\log \frac{\exp(\cosd((\Theta(\alpha_i), \Theta(\alpha_j))/\tau))}{\sum_{k=1}^{2B} I_{[k \neq i]} \exp(\cosd((\Theta(\alpha_i), \Theta(\alpha_k))/\tau))}, \quad (3)$$

where  $\Theta(\cdot)$  represents the network's output,  $\cosd(\mathbf{a}, \mathbf{b}) = \mathbf{a}^T \cdot \mathbf{b} / \|\mathbf{a}\| \|\mathbf{b}\|$  represents the cosine distance between vectors  $\mathbf{a}$  and  $\mathbf{b}$ , and  $\tau$  is a temperature parameter. Then, the whole loss value  $\Psi$  of a mini-batch is defined as

$$\Psi = \frac{1}{2B} \sum_{k=1}^B (\zeta_{2k-1, 2k} + \zeta_{2k, 2k-1}). \quad (4)$$

### E. Classification and Visual Feature Interpretability

The MLP used for the pretext task is replaced by a linear classifier to obtain more generalized feature information in the downstream task. More specifically, this linear classifier is composed of a fully connected layer followed by a softmax function. The network is fine-tuned on a small amount of annotated cervical OCT images by leveraging the features learned in the pre-training process. Finally, it outputs the corresponding probability distributions for the five categories (i.e., MI, EP, CY, HSIL, and CC) and generates a patch label. The likelihood that the input patch belongs to a binary class (i.e., high-risk and low-risk) is inferred by summing up the probabilities over all the categories within the general class.

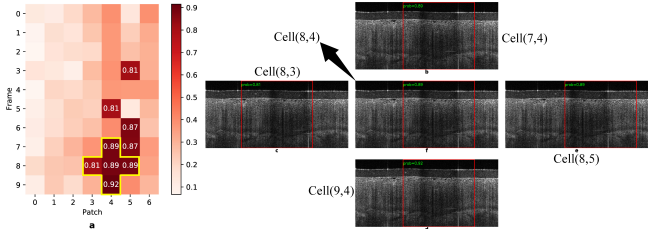


Fig. 2. An illustration of the cross-shaped threshold voting strategy.

For an OCT volume consisting of  $m$  frames, we use slicing windows to extract  $n$  patch from the same frame. As a result, we can obtain a  $m \times n$  matrix of predictions for patches. Furthermore, according to the clinical experience of medical experts, in this study, we design an explainable voting strategy, called cross-shaped threshold voting, to aggregate patch-level predictions into a single result for the whole OCT volume. The basic idea of this strategy is to detect consecutive high-risk patches in the cross-sectional and axial directions, which may look like a cross shape. Moreover, we define a threshold value of 0.8 for high-risk (or positive) to better balance the false-positive and false-negative rates. Fig. 2 illustrates the cross-shaped threshold voting strategy. Our method detected five high-risk patches in this volume, including the fifth patch in the eighth, ninth, and tenth frames and the fourth, fifth, and sixth patches in the ninth frame.

Because the classification model is built using the CNN architecture, we also provide volume- and patch-level feature visualization to assist gynecologists in detecting cervical diseases. For example, for an OCT volume, we present a heat matrix of size  $m \times n$  to help localize a possible lesion (see the left part in Fig. 2). Besides, we use the class activation map (CAM) [23], which generates a heat map highlighting regions most relevant to the corresponding category, to provide better interpretability of diagnoses at the patch level.

## III. EXPERIMENTS AND RESULT ANALYSIS

### A. Experiment Design

To test the performance of our classification model, we designed two groups of experiments: a machine-machine comparison with different deep learning algorithms and a human-machine comparison with medical experts.

**Data partition.** The experimental dataset was randomly divided into a training set and a test set, with an 80:20 split based on the patient identification number, for the two comparison experiments. We applied the ten-fold cross-validation method to the training set for the machine-machine comparison experiment. In addition, we used an external validation dataset to evaluate the robustness of the proposed method. The training set was further divided into two subsets with an 80:20 split in the human-machine comparison experiment. Therefore, 20% of label-free OCT patches in the training set were used for self-supervised learning from scratch and the remaining 80% for the downstream classification task. To avoid the overfitting problem, OCT images from the same patient cannot appear in training and test sets.

**Baselines for comparison.** In the machine-machine comparison experiment, we used VGG19 [24], ResNet-50, and Resnet-101 [25] as our backbone networks. In addition, we trained classification models with different initialization strategies to compare CTL with competitive baselines, including the state-of-the-art contrastive learning method, SimCLR [21], and the supervised learning method for training a model from scratch (denoted as *random initialization*). Moreover, we used EfficientNet-B7 [26] pre-trained on the ImageNet dataset as a supervised pre-training baseline method. Besides, four medical experts from the Third Affiliated Hospital of Zhengzhou University, including one pathologist, one gynecologist, and two radiographers, were involved in the human-machine comparison experiment as anonymous investigators. All of them have learned and used OCT for more than one year.

**Evaluation metrics.** The metric, *accuracy*, was used in both five-class and binary classification tasks. In addition, two frequently-used metrics, i.e., *sensitivity* and *specificity*, were used to evaluate the results in the binary classification task. Also, the area under the ROC curve (AUC) was employed to evaluate a given model's overall performance in the binary classification task. Finally, the machine-machine comparison results were made in terms of the average metric value of the ten-fold cross-validation results.

$$\text{accuracy} = (TP + TN) / (TP + FP + TN + FN), \quad (5)$$

$$\text{sensitivity} = TP / (TP + FN), \quad (6)$$

$$\text{specificity} = TN / (TN + FP), \quad (7)$$

where  $TP$ ,  $FP$ ,  $TN$ , and  $FN$  represent true positives, false positives, true negatives, and false negatives, respectively.

**Environment and Configuration.** The experiments were conducted on an Asus X99-E WS/USB 3.1 workstation with an Intel Xeon E5-2620 v4 (2.10 GHz) and four graphics processing units (NVIDIA GeForce RTX 2080, 7.79 GB). The operating system in the workstation was Ubuntu 16.04, and the programming language was Python 3.6.2. Moreover, we used Pytorch 1.4.0 and scikit-learn 0.24.1 as the basic libraries of deep learning. In the entire pre-training process, we adopted

adaptive gradient descent (Adam) [27] as the optimizer of the network with a  $1e^{-2}$  learning rate and a  $1e^{-6}$  weight decay. The MLP was set as a two-layer densely connected network, with the first layer containing 512 neurons and 128 neurons in the second layer. We adopted stochastic gradient descent (SGD)

[28] as the optimizer with a  $5e^{-3}$  learning rate and a 0.9 momentum for linear classification. The batch size was set to a fixed value of 32 in the two tasks. For more details of the implementation, please refer to the source code available at <https://github.com/whuchris/MIA-CTL>.

TABLE III. COMPARISON AMONG CNN-BASED CLASSIFICATION MODELS (MEAN $\pm$ STD)

Model	Init	Accuracy (%)		Sensitivity (%)	Specificity (%)	AUC
		Five-class	Binary			
VGG19	Random	81.11 $\pm$ 5.96	88.02 $\pm$ 1.70	86.61 $\pm$ 6.30	88.26 $\pm$ 5.71	0.9308 $\pm$ 0.0322
ResNet-50	Random	78.61 $\pm$ 4.91	87.07 $\pm$ 3.17	86.34 $\pm$ 5.36	87.24 $\pm$ 3.81	0.9231 $\pm$ 0.0220
ResNet-101	Random	82.39 $\pm$ 5.11	91.35 $\pm$ 2.84	90.43 $\pm$ 5.55	91.38 $\pm$ 3.64	0.9682 $\pm$ 0.0196
EfficientNet-B7	ImageNet	83.09 $\pm$ 5.93	91.06 $\pm$ 2.78	89.52 $\pm$ 4.82	93.42 $\pm$ 3.11	0.9698 $\pm$ 0.0113
VGG19	SimCLR	82.50 $\pm$ 3.39	90.81 $\pm$ 2.66	88.26 $\pm$ 3.95	90.89 $\pm$ 2.30	0.9644 $\pm$ 0.0248
ResNet-50	SimCLR	83.86 $\pm$ 4.43	91.71 $\pm$ 2.71	89.78 $\pm$ 5.83	93.03 $\pm$ 2.68	0.9723 $\pm$ 0.0161
ResNet-101	SimCLR	82.28 $\pm$ 3.39	91.39 $\pm$ 2.37	<b>92.65<math>\pm</math>4.67</b>	89.25 $\pm$ 4.24	0.9758 $\pm$ 0.0183
VGG19	CTL	84.77 $\pm$ 3.96	91.93 $\pm$ 4.71	90.06 $\pm$ 4.30	92.94 $\pm$ 2.65	0.9725 $\pm$ 0.0145
ResNet-50	CTL	83.63 $\pm$ 4.55	90.54 $\pm$ 1.94	89.60 $\pm$ 3.65	90.54 $\pm$ 4.68	0.9679 $\pm$ 0.0168
ResNet-101	CTL	<b>85.38<math>\pm</math>5.51</b>	<b>92.66<math>\pm</math>1.45</b>	91.17 $\pm$ 4.99	<b>93.96<math>\pm</math>4.72</b>	<b>0.9798<math>\pm</math>0.0157</b>

Init: initialization for pre-training. Random represents that the network was trained from scratch based on a Gaussian distribution, and ImageNet represents that the network was pre-trained on the ImageNet dataset. The number shown in bold indicates the best result in each column.

## B. Results

### 1) Machine-machine comparison for OCT patches

In the five-class classification task, CTL on ResNet-101 achieved the best accuracy of  $85.38\pm5.51\%$  (mean $\pm$ std), followed by CTL on VGG19 with an  $84.77\pm3.96$  accuracy. Compared with SimCLR, the accuracy values of CTL on ResNet-101 and VGG19 were increased by 3.10% and 2.27%, respectively. This result indicates that introducing the texture features of cervical OCT images to contrastive learning can make classification results better. Moreover, the accuracy values of CTL on the three backbone networks were 3.66%, 5.02%, and 2.99% higher than those of supervised learning CNN models without pre-training, respectively. Similarly, the models pre-trained by SimCLR and the ImageNet dataset performed better than those trained from scratch in most cases. This result

suggests that pre-training is helpful to improve the model performance in case of insufficient labeled data.

Table III shows that CTL on ResNet-101 also achieved the best results of accuracy and AUC in the binary classification task. It obtained a  $92.66\pm1.45\%$  accuracy, 1.27% higher than that of SimCLR on ResNet-101. Although the sensitivity of CTL on ResNet-101 is 1.48% lower than that of SimCLR on the same backbone network, it got the highest AUC value of  $0.9798\pm0.0157$ . Moreover, the AUC value of CTL on ResNet-101 is 1% higher than that of the pre-trained EfficientNet-B7. Supervised learning ResNet-101 without pre-training has almost the same AUC value as the pre-trained EfficientNet-B7. Therefore, this result further suggests that contrastive texture feature learning can help improve overall classification performance.

TABLE IV. COMPARISON AMONG MEDICAL EXPERTS AND OUR METHOD (95% CI)

Model&Experts	Accuracy (%)		Sensitivity (%)	Specificity (%)	PPV (%)	NPV (%)
	Five-classes	Binary				
Investigator1	<b>91.58</b> (90.58–92.51)	<b>98.87</b> (98.45–99.20)	97.55 (96.61–98.29)	<b>99.89</b> (99.61–99.99)	<b>99.86</b> (99.48–99.98)	98.14 (97.42–98.70)
Investigator2	86.24 (85.01–87.40)	91.98 (90.99–92.88)	81.95 (79.85–83.91)	99.73 (99.37–99.91)	99.57 (99.10–99.86)	87.73 (86.25–89.10)
Investigator3	88.22 (87.07–89.31)	93.90 (93.02–94.69)	91.74 (90.19–93.2)	95.57 (94.52–96.46)	94.11 (92.75–95.29)	93.74 (92.55–94.79)
Investigator4	87.95 (86.79–89.05)	97.13 (96.50–97.68)	96.16 (96.11–97.09)	97.89 (97.13–98.50)	97.24 (96.25–98.03)	97.06 (96.18–97.77)
Avg. (95% CI)	88.50 (87.36–89.57)	95.45 (94.70–96.16)	91.85 (90.30–93.24)	98.27 (97.57–98.81)	97.70 (96.66–98.37)	94.17 (92.82–94.99)
Ours (95% CI)	87.16 (85.96–88.28)	95.21 (94.42–95.92)	<b>98.53</b> (97.76–99.09)	92.64 (91.36–93.79)	91.19 (89.67–92.56)	<b>98.79</b> (98.15–99.25)

PPV: positive predictive value (TP/(TP+FP)). NPV: negative predictive value (TN/(TN+FN)). CI: confidence interval. CIs for accuracy, sensitivity, specificity, PPV, and NPV are exact Clopper-Pearson confidence intervals at the 95% confidence level [29]. The bold number indicates the best result in each column.

### 2) Human-machine comparison for OCT patches

Table IV presents the comparison results between CTL on ResNet-101 and four medical experts on the test set in the two classification tasks. In the five-class classification task, the accuracy of our method was 1.34% lower than the average of the investigators. Our method achieved almost the same accuracy as the average of the investigators in the binary classification

task. Compared with Investigator1, the best performer, our method's sensitivity and NPV values were increased by  $\sim 1\%$  and 0.65%, respectively. This result indicates that our method has an excellent ability to identify high-risk cervical diseases in OCT images correctly. However, our method's specificity and PPV values were 5.63% lower than the average of the investigators, suggesting that there is room for improvement.

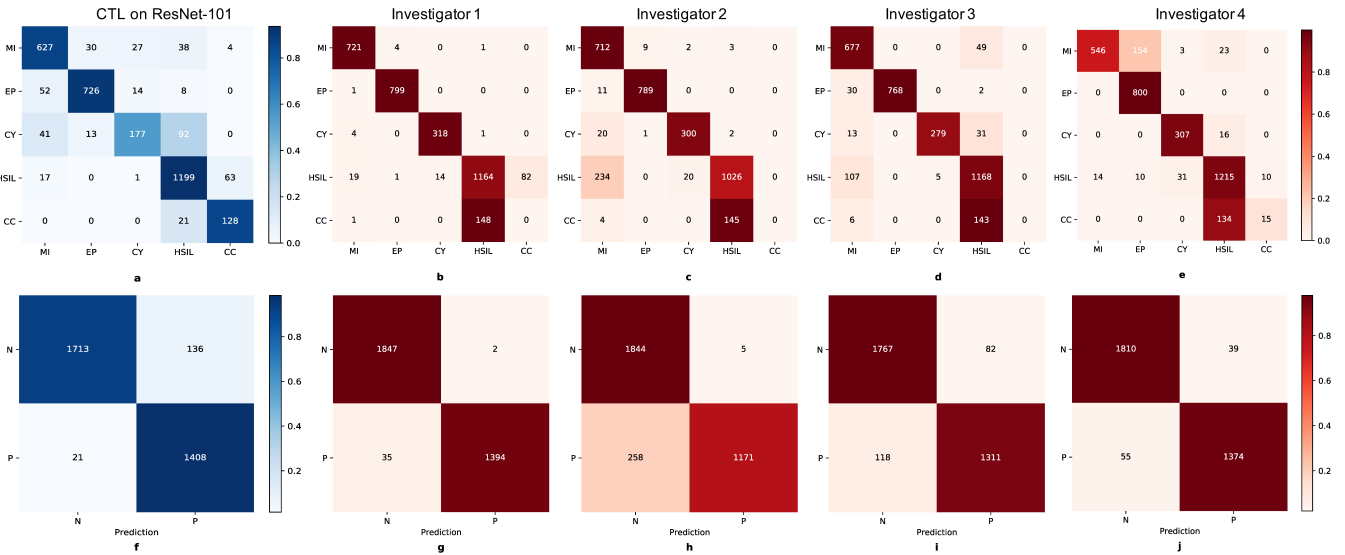


Fig. 3. Confusion matrices of our method and the four investigators. (a)–(e): the five-class classification task; (f)–(j): the binary classification task.

Fig. 3 displays the confusion matrices of our method and the investigators in the human-machine comparison experiment. Our method's false-positive rate was much higher than those of the investigators. The main reason is that a few OCT patches of inflammation and cyst were misclassified by our method as HSIL and cancer, possibly due to similar texture features that are hard to discern. Instead, the investigators' false-negative rates were much higher than that of our method. For example, the best investigator's misclassification rate of high-risk was increased by 9.80% compared with our method. The main reason is that the investigators reviewed patches rather than the entire volume so that they tended to make relatively conservative diagnoses, especially for cervical cancer. Generally speaking, our method reached the average level of the four medical experts and can provide better diagnostic results than the second and third investigators in the binary classification task (see Fig. 4).

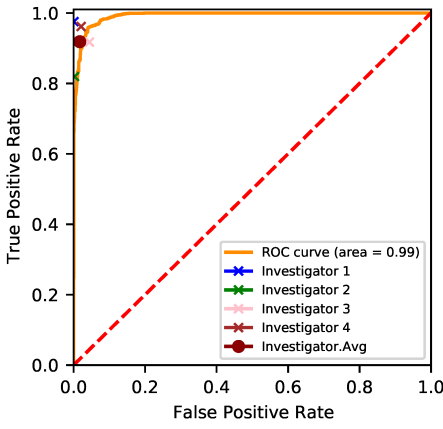


Fig. 4. A ROC curve for the binary classification task.

### 3) External validation for OCT volumes

To evaluate the generalization of our method, we experimented on a different dataset, including 287 cervical OCT volumes from another hospital, a fifth of which were of high risk. Our method outputs a binary classification result for the input OCT volumes using the cross-shaped threshold voting strategy based on patches. Table V shows the classification results on the external validation set and test set. The two datasets are of similar size. As shown in Table V, our CADx method

achieved similar volume-level classification results on the two datasets from different hospitals, suggesting a good capability of robustness and generalization for female patients from different regions. Besides, it is worth noting that the sensitivity value on the external validation set was decreased by 4.83%, suggesting further improvement on our method's ability to deal with intractable cervical lesions in OCT images.

TABLE V. VOLUME-LEVEL CLASSIFICATION RESULTS

Metric	External Validation Set	Test Set
Accuracy (%)	96.17	95.39
Sensitivity (%)	91.53	96.36
Specificity (%)	97.37	95.06
PPV (%)	90.00	86.89
NPV (%)	97.80	98.72

### 4) Feature visualization

In addition to the heat matrix for cervical OCT volumes to localize high-risk lesions, we also used CAM to visualize the learned image features to help gynecologists better interpret the patch-level diagnoses made by our CADx method. Fig. 5 displays six typical cases that belong to ectropion, HSIL, and cervical cancer, and each case contains three types of images: OCT, LBP, and CAM.

The cases of cervical ectropion are placed in the first row of Fig. 5. Although cervical ectropion is a non-cancerous condition for women, sometimes the OCT images of EP are often misclassified as HSIL or cervical cancer by inexperienced gynecologists or pathologists. The OCT images in Fig. 5(a) and 5(b) revealed no layered structure and the papillary structure (PS) with hyper-scattering boundaries in ectropion tissues (see the red arrows). The CAM heatmaps in the first row of Fig. 5 highlighted the papillary structures and interpapillary ridges in the corresponding OCT images, which is consistent with the histomorphological finding in previous studies [5], [6], [8]. Besides, the LBP maps captured sharp contours of ectropion tissues as a noticeable texture feature.

The OCT images in the second row of Fig. 5 demonstrated two cases of HSIL. We cannot find the typical layered structure and the basement membrane in the two cases. Moreover, the image intensity decayed rapidly as the depth of tissue increased, thus forming hyper-scattering icicle-like shapes (see

the regions surrounded by the two red eclipses in Fig. 5(c)) [5]. The OCT image in Fig. 5(d) further presented distinct patterns of light and dark composed of such icicle-like shapes (see the region surrounded by the red eclipse), and the stroma below

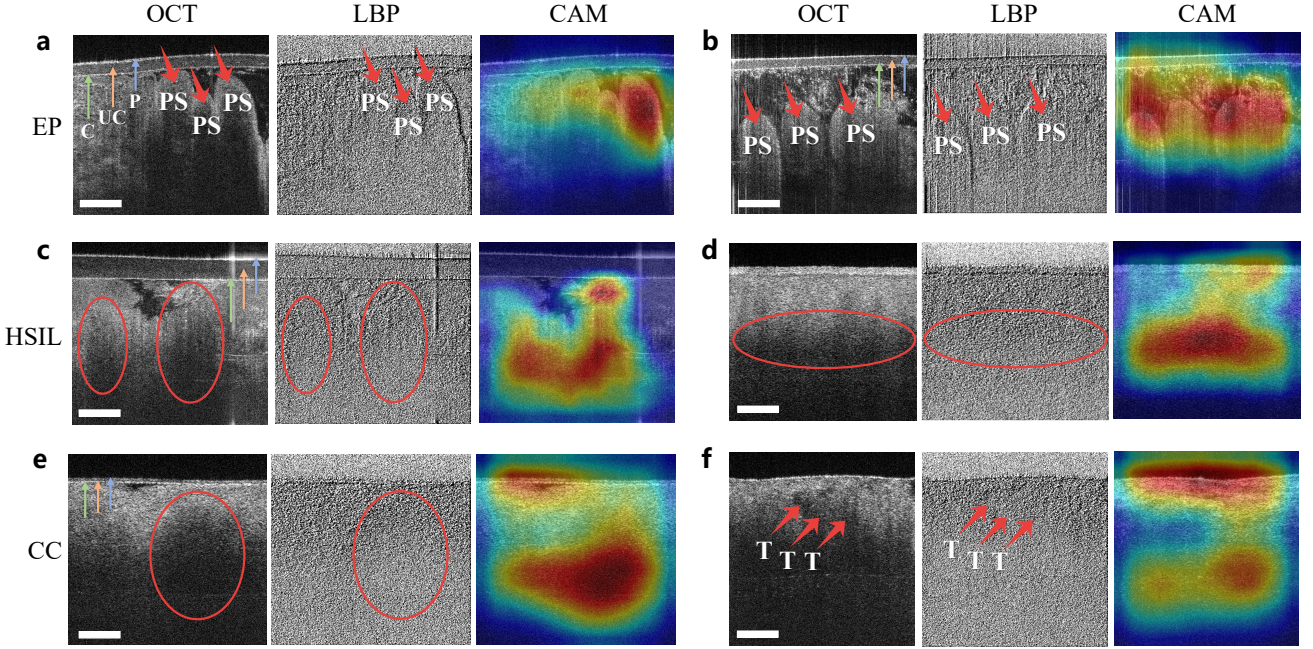


Fig. 5. Pixel-level histomorphological feature visualization. (a) and (b): cervical ectropion; (c) and (d): HSIL; (e) and (f): cervical cancer: squamous cell carcinoma (SCC). PS: papillary structures with hyper-scattering boundaries; T: tumor; C: condom; UC: ultrasound couplants; P: probe. Scale bars: 200  $\mu$ m.

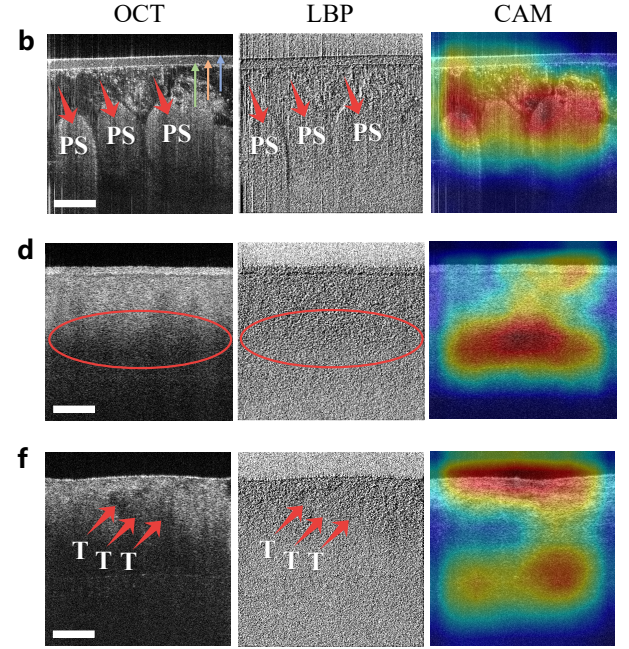
Two cases of cervical cancer (more specifically, squamous cell carcinoma (SCC)) are placed in the third row of Fig. 5. Because the standard squamous epithelial structure and basal membrane were lost entirely, the OCT images revealed a complete lack of architectural polarity [6], [8]. Although the OCT image in Fig. 5(e) shows a pattern similar to HSIL, the image intensity decayed more rapidly and formed hypo-scattering regions surrounded by the red eclipse. In a physical sense, the high density of tumor cells affects light penetration in tumor tissue. The OCT image in Fig. 5(f) presents another pattern, i.e., some irregular nests of heterogeneous regions composed of epithelial cells and tumor cells (see the red arrows) were detected in the epithelial layer. Although the LBP maps provided little explainable evidence for diagnosing SCC, the CAM heatmaps highlighted the histomorphological features of SCC in OCT images recognized in previous studies [5], [8].

#### IV. DISCUSSION

Despite the utilization of self-supervised learning, we experimented with four different sizes of labeled data, i.e., 25%, 50%, 75%, and 100% of the data used for the downstream classification task, to evaluate the impact of labeled data size on prediction performance. Due to limited image data and computing resources, we selected ResNet-101 instead of DenseNet [30] as the backbone network for this experiment. Table VI presents the ten-fold cross-validation results of the backbone network pre-trained with different data sizes

It is evident from Table VI that ResNet-101 with random initialization performed worse in case of insufficient labeled data. For example, ResNet-101 trained by half of the labeled data obtained a  $76.36 \pm 4.74\%$  accuracy in the five-class classification task. Compared with the one trained by all the labeled data, the accuracy value was decreased by  $\sim 6\%$ ; in the binary classification task, the AUC value was decreased by

was no longer observed. The CAM heatmaps also highlighted these histomorphological features [5] in the corresponding OCT images. Unfortunately, the LBP maps show little human-readable texture information to help interpret HSIL.



5.57%. Instead, with the help of self-supervised learning (i.e., CTL and SimCLR), the network's performance can be visibly improved on small-scale training datasets. For example, when using 50% of labeled data, the accuracy values of ResNet-101 trained with CTL and SimCLR were improved by 5.89% and 4.78%, respectively. Moreover, we can see more significant improvement when 25% (or less) of labeled data was available. Therefore, the CTL strategy can help further improve the performance of CNNs for cervical OCT image classification, especially on small-scale datasets of labeled medical images.

TABLE VI. TRAINING ON DIFFERENT SIZES OF LABELED DATA

Size	Classifier	Accuracy (%)	AUC
25%	ResNet-101 (Random)	$53.23 \pm 5.58$	$0.7974 \pm 0.0216$
	SimCLR on ResNet-101	$62.73 \pm 4.79$	$0.8733 \pm 0.0468$
	CTL on ResNet-101	<b><math>66.69 \pm 3.42</math></b>	<b><math>0.8911 \pm 0.0289</math></b>
50%	ResNet-101 (Random)	$76.36 \pm 4.74$	$0.9125 \pm 0.0144$
	SimCLR on ResNet-101	$81.14 \pm 4.07$	$0.9381 \pm 0.0173$
	CTL on ResNet-101	<b><math>82.25 \pm 3.93</math></b>	<b><math>0.9575 \pm 0.0124</math></b>
75%	ResNet-101 (Random)	$78.54 \pm 4.53$	$0.9381 \pm 0.0106$
	SimCLR on ResNet-101	$82.13 \pm 3.65$	$0.9517 \pm 0.0148$
	CTL on ResNet-101	<b><math>83.58 \pm 2.50</math></b>	<b><math>0.9693 \pm 0.0156</math></b>
100%	ResNet-101 (Random)	$82.39 \pm 5.11$	$0.9682 \pm 0.0196$
	SimCLR on ResNet-101	$82.28 \pm 3.39$	$0.9758 \pm 0.0183$
	CTL on ResNet-101	<b><math>85.38 \pm 5.51</math></b>	<b><math>0.9798 \pm 0.0157</math></b>

Accuracy is used for the five-class classification task. The bold number indicates the best result in each group of data sizes.

Low-grade squamous intraepithelial lesion (LSIL), previously known as CIN I, is a low-risk cervical disease. Due to a small number of recruited patients with LSIL, OCT images from LSIL tissues were excluded from the OCT image dataset used in this study. We will update this dataset by adding *in-vivo* OCT volumes of LSIL in the future. Different attention mechanisms have been recently utilized to improve the backbone network's performance for medical images [31]. Therefore, we plan to introduce specific attention mechanisms such

as spatial and channel-wise attention [32] to the classification model. Finally, although we present an explainable voting strategy for cervical OCT volumes, it also has room for improvement. More specifically, we will design a trainable voter using machine learning algorithms to aggregate patch-level prediction results better.

## V. CONCLUSION

We developed a novel CADx method based on self-supervised learning for *in-vivo* 3D OCT volumes from the cervix. In particular, we proposed a contrastive learning strategy based on texture features to pre-train CNN models for cervical OCT image classification. According to the ten-fold cross-validation results on an OCT image dataset from a multi-center clinic study, our method outperformed other competitive models pre-trained from scratch, on the ImageNet dataset, and by a state-of-the-art contrastive learning method, in the five-class and binary classification tasks. Moreover, it performed better than two out of four medical experts on the test set in the binary classification task. Besides, our method demonstrated robustness and generalization for high-risk OCT volumes on the test and external validation sets. Due to better interpretability based on texture features, the proposed CADx method holds great potential to help gynecologists make rapid and accurate diagnoses in the clinical protocol of “see-and-treat.”

## ACKNOWLEDGMENT

This work was supported by the Science and Technology Major Project of Hubei Province in China (Next-Generation AI Technologies) under Grant No. 2019AEA170. In addition, the authors appreciate Tao Xu, Hao Hu, and Di Meng for their valuable work of OCT image collection. Yutao Ma is the corresponding author of this paper.

## REFERENCES

- [1] F. Bray, J. Ferlay, I. Soerjomataram, R. L. Siegel, L. A. Torre, and A. Jemal, “Global cancer statistics 2018: GLOBOCAN estimates of incidence and mortality worldwide for 36 cancers in 185 countries,” *CA Cancer J. Clin.*, vol. 68, no. 6, pp. 394–424, 2018.
- [2] M. Arbyn et al., “Estimates of incidence and mortality of cervical cancer in 2018: a worldwide analysis,” *Lancet Glob. Health*, vol. 8, no. 2, pp. e191–e203, 2020.
- [3] Global strategy to accelerate the elimination of cervical cancer as a public health problem. Geneva: World Health Organization, 2020, pp. 25–31.
- [4] Y. Liu, L. Zhang, G. Zhao, L. Che, H. Zhang, and J. Fang, “The clinical research of Thinprep Cytology Test (TCT) combined with HPV-DNA detection in screening cervical cancer,” *Cell. Mol. Biol.*, vol. 63, no. 2, pp. 92–95, 2017.
- [5] C. Ren et al., “Multi-center clinical study using optical coherence tomography for evaluation of cervical lesions *in-vivo*,” *Sci. Rep.*, vol. 11, Art. no. 7507, 2021.
- [6] Y. Ma et al., “Computer-aided diagnosis of label-free 3-D optical coherence microscopy images of human cervical tissue,” *IEEE Trans. Biomed. Eng.*, vol. 66, no. 9, pp. 2447–2456, 2019.
- [7] D. Huang et al., “Optical coherence tomography,” *Science*, vol. 254, no. 5035, pp. 1178–1181, 1991.
- [8] X. Zeng et al., “Ultrahigh-resolution optical coherence microscopy accurately classifies precancerous and cancerous human cervix free of labeling,” *Theranostics*, vol. 8, no. 11, pp. 3099–3110, 2018.
- [9] J. Gallwas et al., “Detection of cervical intraepithelial neoplasia by using optical coherence tomography in combination with microscopy,” *J. Biomed. Opt.*, vol. 22, no. 1, Art. no. 016013, 2017.
- [10] T. Paczos, A. Bonham, C. Canavesi, J. P. Rolland, and R. O’Connell, “Near-histologic resolution images of cervical dysplasia obtained with Gabor domain optical coherence microscopy,” *J. Low. Genit. Tract. Dis.*, vol. 25, no. 2, pp. 137–141, 2021.
- [11] H. A. Almubarak et al., “Convolutional neural network based localized classification of uterine cervical cancer digital histology images,” *Procedia Comput. Sci.*, vol. 114, pp. 281–287, 2017.
- [12] A. Bhargava, P. Gairola, G. Vyas, and A. Bhan, “Computer aided diagnosis of cervical cancer using HOG features and multi Classifiers,” in *Advances in Intelligent Systems and Computing*, vol. 624, R. Singh, S. Choudhury, and A. Gehlot, Eds. Singapore: Springer, 2018, pp. 1491–1502.
- [13] V. Kudva, K. Prasad, and S. Guruvare, “Hybrid transfer learning for classification of uterine cervix images for cervical cancer screening,” *J. Digit. Imaging*, vol. 33, no. 3, pp. 619–631, 2020.
- [14] S. Priya and N. K. Karthikeyan, “A heuristic and ANN based classification model for early screening of cervical cancer,” *Int. J. Comput. Intell. Syst.*, vol. 13, no. 1, pp. 1092–1100, 2020.
- [15] Z. Alyafeai and L. Ghouti, “A fully-automated deep learning pipeline for cervical cancer classification,” *Expert Syst. Appl.*, vol. 141, Art. no. 112951, 2020.
- [16] Y. Li et al., “Computer-aided cervical cancer diagnosis using time-lapsed colposcopic images,” *IEEE Trans. Med. Imaging*, vol. 39, no. 11, pp. 3403–3415, 2020.
- [17] G. Litjens et al., “A survey on deep learning in medical image analysis,” *Med. Image Anal.*, vol. 42, pp. 60–88, 2017.
- [18] J. Zhu, Y. Li, Y. Hu, K. Ma, S. K. Zhou, and Y. Zheng, “Rubik’s Cube+: A self-supervised feature learning framework for 3D medical image analysis,” *Med. Image Anal.*, vol. 64, Art. no. 101746, 2020.
- [19] A. Taleb et al., “3D self-supervised methods for medical imaging,” in *Proc. NeurIPS 2020*, 2020, [online]. Available: <https://proceedings.neurips.cc/paper/2020/hash/d2dc6368837861b42020ee72b0896182-Abstract.html>.
- [20] L. Chen, P. Bentley, K. Mori, K. Misawa, M. Fujiwara, and D. Rueckert, “Self-supervised learning for medical image analysis using image context restoration,” *Med. Image Anal.*, vol. 58, Art. no. 101539, 2019.
- [21] T. Chen, S. Kornblith, M. Norouzi, and G. E. Hinton, “A simple framework for contrastive learning of visual representations,” in *Proc. ICML 2020*, 2020, pp. 1597–1607.
- [22] T. Ojala, M. Pietikäinen, and T. Mäenpää, “Multiresolution gray-scale and rotation invariant texture classification with local binary patterns,” *IEEE Trans. Pattern Anal. Mach. Intell.*, vol. 24, no. 7, pp. 971–987, 2002.
- [23] B. Zhou, A. Khosla, A. Lapedriza, A. Oliva, and A. Torralba, “Learning deep features for discriminative localization,” in *Proc. IEEE CVPR 2016*, 2016, pp. 2921–2929.
- [24] K. Simonyan and A. Zisserman, “Very deep convolutional networks for large-scale image recognition,” in *Proc. ICML 2015*, 2015, [online]. Available: <https://arxiv.org/abs/1409.1556>.
- [25] K. He, X. Zhang, S. Ren, and J. Sun, “Deep residual learning for image recognition,” in *Proc. IEEE CVPR 2016*, 2016, pp. 770–778.
- [26] M. Tan and Q. V. Le, “EfficientNet: rethinking model scaling for convolutional neural networks,” in *Proc. ICML 2019*, 2019, pp. 6105–6114.
- [27] D. P. Kingma and J. Ba, “Adam: a method for stochastic optimization,” *arXiv.org*, arXiv:1412.6980, 2014, [online]. Available: <https://arxiv.org/abs/1412.6980>.
- [28] I. Sutskever, J. Martens, G. E. Dahl, and G. E. Hinton, “On the importance of initialization and momentum in deep learning,” in *Proc. ICML 2013*, Cycle 3, 2013, pp. 1139–1147.
- [29] C. J. Clopper and E. S. Pearson, “The use of confidence or fiducial limits illustrated in the case of the binomial,” *Biometrika*, vol. 26, pp. 404–413, 1934.
- [30] G. Huang, Z. Liu, L. van der Maaten, and K. Q. Weinberger, “Densely connected convolutional networks,” in *Proc. IEEE CVPR 2017*, 2017, pp. 2261–2269.
- [31] H. Sun, X. Zeng, T. Xu, G. Peng, and Y. Ma, “Computer-aided diagnosis in histopathological images of the endometrium using a convolutional neural network and attention mechanisms,” *IEEE J. Biomed. Health Informatics*, vol. 24, no. 6, pp. 1664–1676, 2020.
- [32] L. Chen et al., “SCA-CNN: Spatial and Channel-Wise attention in convolutional networks for image captioning,” in *Proc. IEEE CVPR 2017*, 2017, pp. 6298–6306.